Operando Stability Studies of Ultrathin Single-Crystalline IrO_2(110) Films under Acidic Oxygen Evolution Reaction Conditions

Tim Weber[1,2], Vedran Vonk[3], Daniel Escalera-López[4], Giuseppe Abbondanza[5], Alfred Larsson[5], Volkmar Koller[1,2], Marcel J.S. Abb[1,2], Zoltan Hegedüs[3], Thomas Bäcker[3], Ulrich Lienert[3], Gary S. Harlow[6], Andreas Stierle[3,7], Serhiy Cherevko[4], Edvin Lundgren[5], Herbert Over[1,2,*]

1) Institute of Physical Chemistry, Justus Liebig University, Heinrich-Buff-Ring 17, 35392 Giessen, Germany
2) Center for Materials Research, Justus Liebig University, Heinrich-Buff-Ring 16, 35392 Giessen, Germany
3) Deutsches Elektronensynchrotron (DESY), Notkestr. 85, 22607 Hamburg, Germany
4) Helmholtz Institute Erlangen-Nürnberg for Renewable Energy (IEK-11), Forschungszentrum Jülich GmbH, Egerlandstr. 3, 91058 Erlangen, Germany
5) Synchrotron Radiation Research, Lund University, 22100 Lund, Sweden
6) Department of Chemistry, Nano-Science Center, University of Copenhagen, Universitetsparken 5, 2100 Copenhagen, Denmark
7) Fachbereich Physik, University Hamburg, 20355 Hamburg, Germany

* Corresponding author: Email: over@uni-giessen.de

Abstract:
The anodic corrosion behavior of 50 Å thick single-crystalline IrO_2(110) films supported on slightly bulk-reduced TiO_2(110) single crystals is studied during acidic water splitting by a unique combination of operando techniques, namely, synchrotron-based high-energy x-ray reflectivity (XRR) and surface x-ray diffraction (SXRD) together with highly-sensitive inductively coupled plasma mass spectrometry (ICP-MS). Corrosion-induced structural and morphological changes of the IrO_2(110) model electrode can be followed on the atomic scale by operando XRR and SXRD that is supplemented with ex situ scanning tunneling microscopy (STM) and x-ray photoelectron spectroscopy (XPS), whereas with ICP-MS the corrosion rate can be quantified down to 1 $pg \cdot cm^{-2} \cdot s^{-1}$ with a time resolution on the second scale. The operando synchrotron-based x-ray scattering techniques are surprisingly sensitive to Ir corrosion of about 0.10 ML IrO_2(110) in ≈26 h, i.e. 0.4 $pg \cdot cm^{-2} \cdot s^{-1}$. The present study demonstrates that single-crystalline IrO_2(110) films are much more stable than hitherto expected. Although the dissolution rate is very small, ICP-MS experiments reveal a significantly higher dissolution rate than the operando high energy XRR/SXRD experiments. These differences in dissolution rate are suggested to be due to the different modi operandi encountered in ICP-MS (dynamic) and operando XRR/SXRD experiments (steady state), a fact that may need to be considered when hydrogen production is coupled to intermittent energy sources such as renewables.

Keywords: IrO_2; single-crystalline model electrodes; operando studies; oxygen evolution reaction (OER); electrocatalyst stability; HESXRD; XRR; SFC-ICP-MS;

1. Introduction

A major challenge for renewable energy sources such as wind, solar, and tidal is their intermittent availability and the requirement to store excess energy in periods of high supply in chemical energy. In this context, water electrolysis is expected to become a cornerstone for sustainable energy conversion from electric renewable energies to molecular hydrogen.[1,2] Hydrogen can either be employed directly as a basic chemical in several large-scale industrial processes including steel production and ammonia synthesis, or hydrogen can serve as a central energy carrier where energy conversion devices such as fuel cells transform the energy stored in the hydrogen bond back into electric energy.

Currently, two technologies of water electrolysis are in operation, working either in alkaline or in acidic environments.[3] Alkaline electrolyzers are technically and economically mature for operation under steady state conditions, but unfortunately are not able to cope with the fluctuating energy supply of renewable sources. Acidic water electrolyzers with polymer electrolyte membrane (PEM) offer several advantages over alkaline electrolyzers, including high current densities, high efficiency for the hydrogen evolution reaction (HER), and most importantly can run under dynamic operation conditions.[4] The HER takes place at the cathode (consisting of well-dispersed Pt particles) with high efficiency, while severe efficiency losses in these devices are traced to the sluggish counter reaction at the anode, that is the oxygen evolution reaction (OER).[5] Besides high activity of an OER electrocatalyst, long-term stability over the whole lifetime of the electrolyzer is a major concern, not only because the anode operates at oxidizing potentials, but also as a result of the acidic electrolyte of PEM electrolyzers. Most investigated OER electrocatalysts have been found to undergo substantial corrosion during acidic OER.[6] At present, only the precious metal oxides based on IrO_2 and RuO_2 show reasonable activity and stability under the harsh reaction conditions,[7] and currently there are no adequate substitutes in sight.[8] Since IrO_2 is much more stable than RuO_2, IrO_2 is currently employed in PEM water electrolyzers.[9] Nevertheless, IrO_2 corrodes, albeit slowly, under such harsh reaction conditions.

Over the past decade, atomistic insight into the OER over transition metal oxides has advanced thanks to ab initio theory[10,11] and dedicated model experiments.[12-14] With universal scaling relations in theory[15] it is possible to rationally screen for improved OER catalysts in terms of activity. A similar level of atomic-scale understanding of the anodic corrosion and dissolution has yet to be developed. Missing are clear-cut experiments based on suitable model systems that would advance theoretical modeling.[16] Fundamental studies based on single-crystalline model electrodes can help us understand such processes on the nanoscale and may pave the way for a rational search to substitute scarce and expensive iridium.

Microscopic studies of corrosion processes are just emerging: Most studies quantify the amount of metals dissolved either by microbalance[17] or by highly-sensitive inductively coupled plasma mass spectrometry (ICP-MS)[18]. With these studies the dissolution rate can be quantified, important information indeed. However, these studies cannot provide information on the chemical nature of the dissolving species nor microscopic insights into the corrosion process at the anode. Recently, Zagalskaya and Alexandrov[19] presented a first attempt towards molecular understanding of the dissolution process at the IrO_2(110) surface. Under OER conditions the surface-bound IrO_2OH species was found to be thermodynamically quite stable and to undergo transformation to IrO_3 that was identified with the dissolution product of a polycrystalline IrO_2 film.[20]

Weber et al.[21,22] employed single-crystalline model electrodes for stability studies under acidic OER conditions. This work studied the corrosion of ultrathin single-crystalline IrO_2(110) films (100 Å thick) coated on RuO_2(110)/Ru(0001). It was shown that IrO_2(110) served as a protecting layer for the underlying RuO_2(110)/Ru(0001) substrate that is much less stable against corrosion than the covering IrO_2(110) film. Therefore, at anodic potentials of 1.48 V vs. the standard hydrogen electrode (SHE) potential-induced pitting corrosion was observed and dominated the corrosion behavior.

In this report a ultrathin single-crystalline IrO_2(110) film is supported on an inert TiO_2(110) substrate in order to avoid pitting corrosion and to follow corrosion-induced structural and morphological changes of the IrO_2(110) layer on the atomic scale by employing a unique and powerful combination of operando techniques. The thickness of the IrO_2(110) film is chosen to be about 50 Å so that even subtle structural and morphological changes can be identified with operando x-ray reflectivity (XRR) and high-energy surface x-ray diffraction (HESXRD) as well as with ex situ high fidelity imaging techniques such as scanning tunneling microscopy (STM). The corrosion rate of single-crystalline IrO_2(110)-TiO_2(110) is quantified with complementary highly-sensitive scanning flow cell-inductively coupled plasma mass spectrometry (SFC-ICP-MS).

2. Experimental Section

2.1 Sample preparation and characterization

The IrO_2(110)-TiO_2(110) model electrodes were prepared under ultrahigh-vacuum (UHV) conditions by depositing single-crystalline IrO_2(110) ultrathin films onto TiO_2(110) single crystals (hat-shaped disks, 4.7 mm diameter; MaTecK, Jülich, Germany), as described previously.[23] To ensure a sufficiently high electronic conductivity of the samples, the TiO_2(110) single crystal was reduced by thermal annealing under UHV conditions. Subsequently, the bulk-reduced TiO_{2-x}(110) sample was cleaned by repeated cycles of Ar^+ ion sputtering (p(Ar) = 10^{-6} mbar, U = 1.0 - 1.5 kV, $I_{emission}$ = 20 mA) and subsequent annealing in an oxygen atmosphere (T = 950 K, $p(O_2)$ = 10^{-7} mbar). Thereafter, the sample surface was mildly re-oxidized in an oxygen atmosphere of $5 \cdot 10^{-6}$ mbar at 950 K for 1 min, resulting in a TiO_2(110) surface while preserving the degree of reduction in the bulk material. On this TiO_2(110)/TiO_{2-x}(110) sample, iridium was deposited and oxidized stepwise in an oxygen atmosphere of 10^{-6} mbar at 700 K via physical vapor deposition (PVD) employing a well-outgassed electron beam evaporator (EFM 3, Omicron). For convenience, these IrO_2(110)-TiO_2(110)/TiO_{2-x}(110) samples are referred to as IrO_2(110)-TiO_2(110) model electrodes throughout the manuscript. After preparation, the model electrode surfaces were characterized by x-ray photoelectron spectroscopy (XPS) and scanning tunneling microscopy (STM). XPS experiments were conducted with a photon energy of 1253.6 eV (Mg Kα line) and a hemispherical analyzer (PSP Vacuum Technology) while for STM experiments a VT-STM (Omicron) was utilized.

Reactively sputtered IrO_2 oxide was deposited at 100 W (BESTEC GmbH, Berlin, Germany) in a mixture of O_2 and Ar as the sputter gas and the chamber pressure was adjusted to 0.5 Pa at room temperature. The resulting thickness of the obtained coating was approximately 100 nm. To prepare films with a minimal surface roughness, on the smooth substrates of single crystalline Si(100) wafers with a 1.5 µm thermal SiO_2 diffusion and reaction barrier layer were used. The Ø3 inch target of Ir (99.9%, Evochem, Germany) was pre-cleaned by sputtering prior to deposition.

2.2 Operando electrochemical dissolution measurements

IrO_2(110)-TiO_2(110) model electrodes were subject to SFC-ICP-MS experiments,[24] where the SFC setup was operated with a LabVIEW controlled Gamry Reference 600 potentiostat (Gamry, USA) and coupled downstream to a Perkin Elmer NexION 300x ICP-MS. Prior to electrochemical experimentation, the ICP-MS was calibrated with freshly prepared standard solutions containing defined amounts of elemental Ir and Ti (0.5 to 5 µg L^{-1}, Merck Certipur) along with 10 µg·L^{-1} ^{187}Re and ^{45}Sc as internal standards. The V-shaped scanning flow cell, manufactured from a polycarbonate block (CAM 4-02 Impression Gold, vhf camfacture AG, Germany), presented an oval-shaped cross-section of 0.033 cm^2 which acted as the working electrode area. Besides the SFC, the three-electrode electrochemical setup comprised a double-junction Ag/AgCl reference electrode compartment (Metrohm, Switzerland; 0.1 M $HClO_4$ filling in outer junction, 3 M KCl electrolyte filling in inner junction) and a graphite rod counter electrode compartment (6 mm diameter, 99.995 %, Sigma-Aldrich). The 0.1 M $HClO_4$ electrolyte employed (70 %, Suprapur grade, Merck; pH = 1), freshly prepared with ultrapure water (MilliQ IQ 7000, Merck), was pumped through the SFC setup with Tygon tubing (ID = 380 µm) flowing downstream towards the ICP-MS peristaltic pump at a flow rate of 203 µL·min^{-1}.

Before and after the SFC-ICP-MS experiments, the model electrodes were characterized via scanning electron microscopy (SEM) and XPS. For the XPS characterization, a PHI VersaProbe II instrument was employed which due to an x-ray spot size of ≈200 µm allows to discriminate between the electrochemically treated and non-treated areas of the electrode surface. The measurements were conducted with a photon energy of 1486.6 eV (Al Kα line). SEM experiments were conducted within a Merlin apparatus (Zeiss) using an acceleration voltage of 2 kV and a probe current of 115 pA.

2.3 Synchrotron-based operando x-ray diffraction and scattering studies

Operando HESXRD and XRR experiments were carried out at the Swedish Materials Science beamline P21.2 at PETRA III, DESY, Hamburg, Germany. High-energy x-rays allow for penetrating chamber walls and non-ambient sample surroundings, like in this case a liquid electrolyte. In addition, the relatively small diffraction angles in combination with large area detectors enable us to record large portions of reciprocal space in relatively short time spans.[25,26] Here, two large flat panel x-ray detectors were employed, which resulted in the recording up to relatively high-indexed Bragg reflections, like (333), which are very sensitive to any structural changes on the atomic scale. In addition, this measurement scheme provides crystal truncation rods (CTRs), which contain atomic scale crystallographic information from the interfaces. All these diffraction signals combined allow us to follow the electrode's stability on the atomic scale. A monochromatic, microfocused beam was used with an x-ray energy of 67.15 keV (λ = 18.46 pm) and dimensions of 7×2 μm^2 (horizontally×vertically). The distance between the sample and two Varex 4343CT flat panel detectors was 2.414 m. A standard LaB_6 powder was used for calibration of several diffraction parameters, such as wavelength and sample-detector distance. The x-ray beam impinged the sample surface at a grazing angle of 0.03 degrees, which is slightly below the critical angle for total external reflection. After alignment of the surface normal parallel to the main diffractometer axis, diffraction data are collected during a 180 degree rotation about this axis, which does not change the grazing incidence geometry. Individual IrO_2(110) Bragg reflections were analyzed with a smaller region

of interest around them. Locally the background was determined to obtain background-subtracted integrated intensities. In addition, the positions and widths of these Bragg peaks were analyzed in the $q_{||}$ and $q_{\perp}$ directions, which give information about the crystal structure in the in- and out-of-plane directions, respectively. The full power of the operando high energy SXRD/XRR technique is only achieved in case of well-defined single-crystalline ultrathin films (5nm). With polycrystalline IrO_2 films (prepared by reactive sputtering) we would not reach the required sensitivity due to a thickness of 100 nm and the required sample quality. The sputtered IrO_2 coatings are not very flat and most notably, the film is polycrystalline so that diffraction will lead to powder rings.

For the stability studies under OER conditions, a dedicated electrochemical flow cell setup was employed which consisted of a specifically constructed electrochemical cell[27,28] connected to an electrolyte reservoir and a peristaltic pump to enable permanent flushing of the cell with new electrolyte solution. The IrO_2(110)-TiO_2(110) model electrode serving as working electrode is situated at the bottom of the electrochemical cell while the glassy carbon counter electrode is located at its top. The Ag/AgCl reference electrode is placed in between the working and counter electrodes. As electrolyte solution a 0.5 M H_2SO_4 solution (pH 0.4) was used, prepared from concentrated sulfuric acid (96 %, Suprapur grade; Merck, Darmstadt, Germany) and high-purity water. A PGSTAT204 instrument (Autolab-Metrohm) was employed as galvanostat. This kind of experimental set-up is now accessible for general users of PETRA III (request can be directed to NanoLab at PETRA III).

First, HESXRD and XRR characterization of the IrO_2(110)-TiO_2(110) model electrode was conducted at open-circuit potential (OCP) in 0.5 M H_2SO_4 solution. The HESXRD data were collected via rotation of the sample by 180 degree around its surface normal in the x-ray beam. When this rotational scan was finished the flat panel detectors were translated out of the direct beam to allow the XRR scans via an automated procedure (≈ 1 min). After recording XRR data the detectors were moved back again. A rotational scan and a XRR scan took about 15 min each. Subsequently, the model electrode was subject to a galvanostatic hold at 50 $mA \cdot cm^{-2}$ during which operando HESXRD and XRR data were recorded occasionally in order to keep the photon exposure low.

After the beamtime, the model electrode surface was post-characterized by STM and XPS employing the instruments and parameters as described in the *Sample preparation and characterization* section. The sample transfer from the beamtime to the STM/XPS chamber proceeded through ambient pressure.

3. Experimental Results

3.1 SFC-ICP-MS experiments on IrO_2(110) dissolution

The dissolution rate of Ir for the IrO_2(110)-TiO_2(110) model electrode was quantified via SFC-ICP-MS. The electrochemical protocol (cf. **Figure 1a**) started with bringing the electrode surface into contact with the SFC followed by 6 min at OCP. Subsequently, seven consecutive galvanostatic holds (also termed *OER pulses*) at 5 $mA \cdot cm^{-2}$ for 30 s each were applied, with the holds being separated by 4 min each at OCP; one monolayer of IrO_2(110) corresponds to 370 $ng \cdot cm^{-2}$ of IrO_2.The complete electrochemical protocol was carried out at the same SFC spot. The results of the SFC-ICP-MS measurements are summarized in **Figure 1**. The electrochemical protocol was applied also to a polycrystalline reactively-sputtered IrO_2 electrode similar to that used in refs.[18,20]. With a comparison of single-crystalline versus polycrystalline IrO_2 the effect of polycrystallinity on the corrosion rate can be estimated.

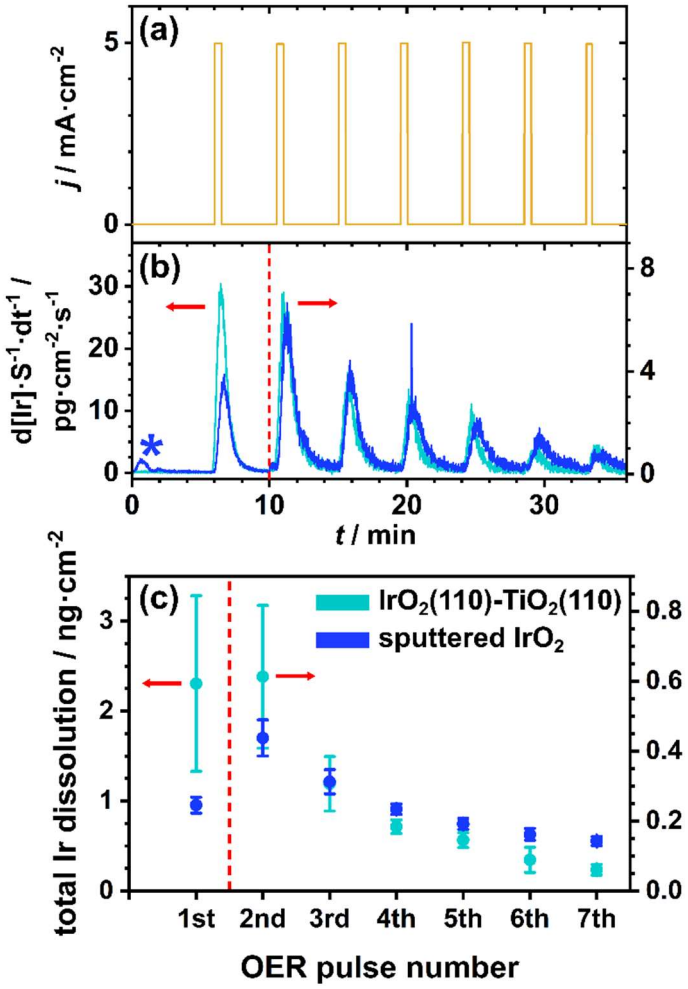

Figure 1: Summary of the SFC-ICP-MS experiments on $IrO_2(110)$-$TiO_2(110)$ and sputtered IrO_2. (a) Electrochemical protocol of consecutive galvanostatic holds (OER pulses), (b) monitored Ir dissolution rate at the ICP-MS, and (c) total amount of Ir dissolution depending on the OER pulse number. The asterisk in (b) indicates the dissolution peak of the sputtered IrO_2 electrode upon contact with the electrolyte. The dissolution rate and the total dissolution of the second and higher OER pulse in (b) and (c), respectively, are displayed on a different scale (cf. dashed red line and red arrows).

Figure 1a displays the electrochemical protocol employed, while in **Figure 1b** the resulting Ir dissolution rates are shown for $IrO_2(110)$-$TiO_2(110)$ and polycrystalline sputtered IrO_2. After the SFC has been brought into contact with the electrode surface, a small dissolution peak emerges in case of the sputtered IrO_2 (cf. **Figure 1b**, blue asterisk), indicating dissolution of intrinsically unstable surface defects or native oxides[29], while for $IrO_2(110)$-$TiO_2(110)$ (cf. **Figure 1b**, cyan line) no such dissolution peak is discernible, compatible with the defect-free nature of the $IrO_2(110)$ film. When applying the first and second OER pulse at 5 $mA \cdot cm^{-2}$ the total amount of Ir dissolution detected is, respectively, two-fold (2.3 ± 1 vs. 0.95 ± 0.09 $ng \cdot cm^{-2}$) and 1.5-fold (0.6 ± 0.2 vs. 0.44 ± 0.05 $ng \cdot cm^{-2}$) higher for $IrO_2(110)$-$TiO_2(110)$ than for sputtered IrO_2. This difference is due most likely to residual metallic Ir on the surface.[30] From photoelectron spectroscopy we can estimate that about 1 % of a monolayer of Ir is present on the surface; this amount to about 3.7 ng/cm^2. From ICP-MS the total amount of the first three pulses adds up to 3.2 ng/cm^2 which is in agreement with the photoelectron spectroscopy study. However, for the third OER pulse the amount of Ir dissolution becomes virtually identical for both electrodes while above the fourth pulse the $IrO_2(110)$-$TiO_2(110)$ model electrode is significantly more stable than the sputtered IrO_2 electrode: at the fourth pulse, the total amount

of Ir dissolution of the IrO_2(110)-TiO_2(110) electrode (0.18 ± 0.02 ng·cm^{-2}) is less than for the sputtered IrO_2 (0.23 ± 0.02 ng·cm^{-2}, cf. **Figure 1c**). A trend of stabilization, i.e., the decrease of total amount of Ir dissolution with increasing number of consecutive OER pulses, is clearly visible for both electrodes. For the IrO_2(110)-TiO_2(110) model electrode, dissolution decreases by almost two orders of magnitude from 2.3 ± 1 ng·cm^{-2} after the first OER pulse to 0.06 ± 0.02 ng·cm^{-2} after the seventh pulse, while in case of the sputtered IrO_2 electrode the decrease is one order of magnitude from 0.95 ± 0.09 ng·cm^{-2} to 0.14 ± 0.01 ng·cm^{-2}.
After the SFC-ICP-MS experiments, the electrochemically treated areas of the model electrode surface were characterized by means of SEM and XPS (cf. Section 1 of the SI). No corrosion-induced changes are discernible.

3.2 Operando HESXRD and XRR studies

The diffraction of x-rays by surfaces results in diffraction patterns consisting of Bragg peaks and streaks of intensity, so-called crystal truncation rods (CTRs), connecting these peaks. Discrete Bragg peaks arise from the single-crystalline materials in the beam (the TiO_2(110) substrate and the covering IrO_2(110) ultrathin film). Since it has been shown previously that the lattice parameters of the (110)-oriented TiO_2 unit cell (a = c = 6.496 Å, b = 2.959 Å, and α = β = γ = 90°) are not completely adopted by the IrO_2(110) film, i.e. the film exhibits a non-pseudomorphous growth (a = c = 6.44 Å, b = 3.05 Å, and α = β = γ = 90°),[31] the TiO_2(110) and IrO_2(110) Bragg peaks and CTRs can be discriminated. The lattice parameters of IrO_2(110) do not vary with the film thickness. Experiments on the IrO_2(110)-TiO_2(110) model electrode surface mainly show CTRs from the TiO_2(110) substrate, the CTRs arising from the IrO_2(110) film are more diffuse and weaker due to the anisotropic ultrathin film microstructure. It is beneficial for the signal-to-noise ratio to use a geometry in which the incoming x-ray beam impinges at a grazing angle onto the surface. Here, the x-rays transit the ambient liquid electrolyte, and when the incidence angle is close to the angle for total external reflection, the penetration into the TiO_2(110) substrate is minimized. This enables unwanted background scattering from the substrate (for example, thermal diffuse scattering) to be minimized. However, the diffraction pattern is still dominated by the very strong TiO_2(110) Bragg reflections which need to be locally shielded as the detector has only a limited dynamic range. In this way it is possible to observe the much weaker CTR signals and IrO_2(110) Bragg reflections on the detector. Despite this nuisance, the use of multiple large area detectors allows for sampling a large part of reciprocal space, including the very weak CTRs, in a relatively short time span (~15 minutes).[25]
Diffraction patterns were collected as a function of time during a galvanostatic hold at 50 mA·cm^{-2} (operando HESXRD). A typical diffraction pattern and a corresponding in-plane diffraction map can be found in Section 2 of the SI (cf. **Figure S3**). To assess the stability of the IrO_2(110)-TiO_2(110) model electrode under OER conditions, the intensities, positions, and widths of several IrO_2(110) Bragg reflections were recorded and evaluated as a function of time. Additionally, operando XRR measurements were conducted at regular intervals to monitor the thickness of the IrO_2(110) film as a function of time. In the context of the present study, (HE)SXRD and XRR are complementary methods: XRR allows us to follow a "homogeneous" dissolution of the IrO_2(110) film, i.e. layer-by-layer dissolution, while with the intensity of the diffraction spots in (HE)SXRD allows "heterogeneous" dissolution to be followed. Combining (HE)SXRD and XRR therefore enables us to obtain a more complete picture of possible structural changes of the model electrode during OER.

All recorded XRR scans can be found in **Figure S4** in the SI. A basic evaluation of the XRR data is based on the oscillation period Δq between two consecutive maxima or minima in the XRR scan: the film thickness d is given by $d = \frac{2\pi}{\Delta q}$, with q being the momentum transfer $q = \frac{4\pi}{\lambda}\sin\theta$, θ being half the scattering angle, and λ being the wavelength of the x-rays. At OCP in 0.5 M H_2SO_4 (cf. **Figure S4**; OCP ≈ 0.67 V vs. the reversible hydrogen electrode (RHE)), a film thickness of 50 ± 1 Å can be derived which does not vary throughout the galvanostatic hold at 50 mA·cm^{-2} over ≈26 h since the position of the maxima and minima of the oscillations are preserved. In addition, all XRR scans were fitted employing the software package GenX[32] (v. 2.4.10) within a simple one-layer model[31] and exemplified in **Figure 2a** for XRR scans at OCP and after ≈26 h of the galvanostatic hold. In **Figure 2b** the IrO_2(110) film thickness is shown as a function of time within the galvanostatic hold that is derived from simulations of the complete set of XRR scans. Further details on the fitting parameters and procedure can be found in **Table S2**.

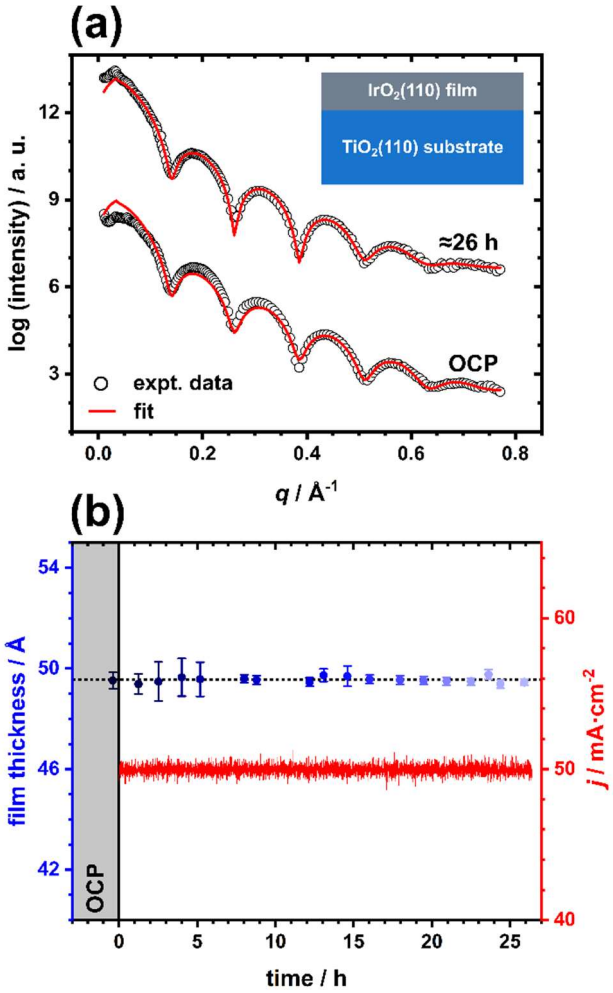

Figure 2: (a) Comparison of experimental (black hollow circles) and fitted (red line) XRR data at OCP and after ≈26 h of the galvanostatic hold at 50 mA·cm^{-2}. The inset in (a) schematically depicts the one-layer model employed to fit the XRR data. (b) Film thickness as derived by fitting of the XRR data (blue-colored circles) and applied current density (red line) as a function of polarization time. The black dotted line displays the average value of the film thickness. The light gray area indicates the data recorded at OCP. Time zero is referenced to the start of the galvanostatic hold.

The fitting reveals the thickness of the IrO_2(110) film to be 49.5 Å both at OCP and after ≈26 h of oxygen evolution at 50 mA·cm^{-2}, only the roughness of the film seems to have increased

slightly from 3.0 Å to 3.9 Å, respectively (cf. **Table S2**). This value for the roughness is in very good agreement with previous studies[31] and shows the excellent structural quality of the electrode preparation to be highly reproducible. Therefore, we infer that the thickness of the IrO_2(110) film has not been altered after oxygen evolution for ≈26 h at a current density of 50 mA·cm^{-2}. A linear regression of thickness data in **Figure 2b** evidences that the thickness of the IrO_2(110) layer is preserved within an uncertainty of ±0.1 Å: 49.6 ± 0.1 Å.

Since XRR is not sensitive to the crystallinity of a film and rather insensitive to "heterogeneous" dissolution phenomena (like potential-induced pitting corrosion[21]), the integrated intensities, peak positions, and FWHM (full width at half maximum) values of IrO_2(110) Bragg reflections in the HESXRD experiments were monitored throughout the galvanostatic hold (cf. **Figure 3**). Further plots for additional reflections can be found in the SI (cf. **Figure S5**). The integrated intensity of a reflection scales with the number of unit cells. So, as soon as the number of scatterers decreases or disorder in the film increases, due to anodic corrosion, the integrated intensity will decline. As can be seen from **Figure 3a-c** the intensities of the (022), (113), and (224) reflections from the IrO_2(110) ultrathin film do not significantly differ from their values at OCP during the ≈26 h galvanostatic hold. This must mean that the number of unit cells does not change and therefore the crystallinity of the IrO_2(110) film remains intact. The intensity variation during polarization was less than 2% of the integrated intensity with no clear trend; we attribute the scattering in the intensities to slight variations of the sample alignment in the beam. This translates to a variation in the IrO_2(110) film thickness of less than 0.3 monolayers (ML). In addition, the position of the (022), (113), and (224) reflections in 2θ and their FWHM values (degree 2θ) are plotted as a function of time in **Figure 3d-i**. Both the position in 2θ and the FWHM values in-plane (ip) and out-of-plane (oop) of the reflection are fairly constant over time within the galvanostatic hold, indicating that the lattice constants and crystallite sizes in the IrO_2(110) film are not affected by the electrochemical treatment.

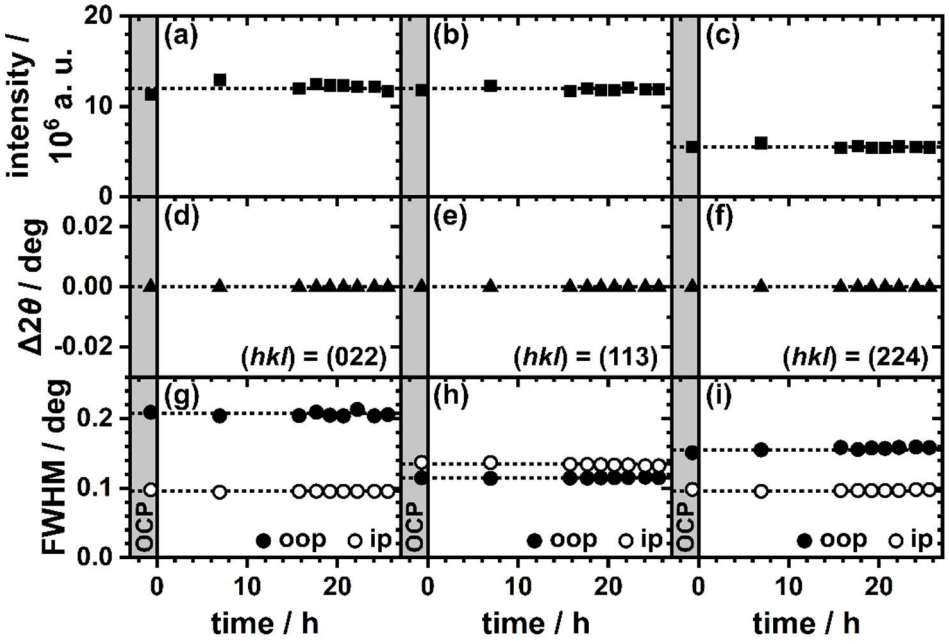

Figure 3: (a)-(c) Integrated intensities, (d)-(f) shift in peak position Δ2θ, and (g)-(i) FWHM values of the IrO_2(110) (022), (113), and (224) reflections as a function of time for the galvanostatic hold of 50 mA·cm^{-2}. The FWHM values are given for the in-plane (ip) and out-of-plane (oop) directions by hollow and filled circles, respectively. The grey area indicates the data recorded at OCP, time zero is referenced to the start of the galvanostatic hold.

Recent characterization of a IrO_2(110)-TiO_2(110) model electrode under cathodic conditions in the HER potential region[31] revealed so-called Laue oscillations in the CTRs. Similar Laue fringes can be observed here, for instance, for the (2,0) CTR which is depicted in **Figure 4** for various polarization times indicated. In addition, the (0,2) CTR is shown in **Figure S6**.

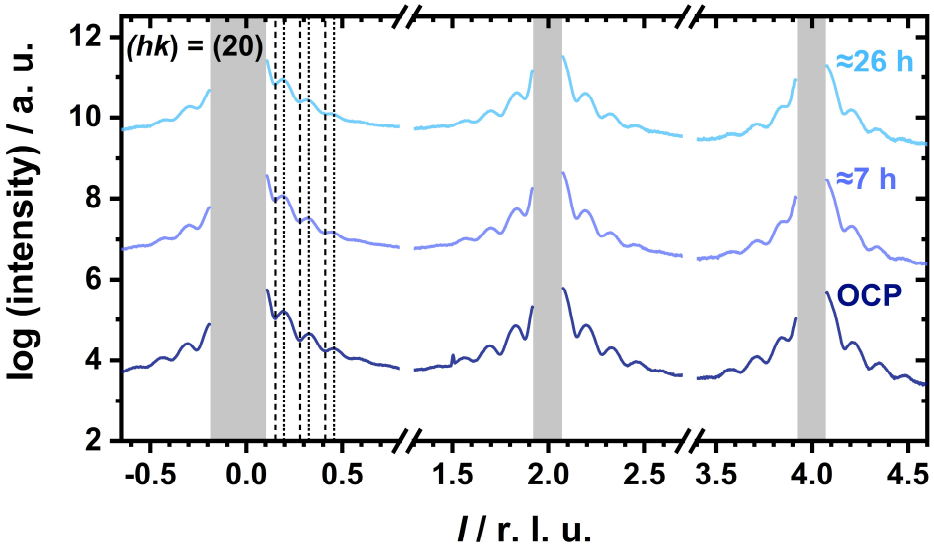

Figure 4: Crystal truncation rods at (*hk*) = (20) for varying conditions: OCP (dark blue), ≈7 h at 50 mA·cm^{-2} (blue), and ≈26 h at 50 mA·cm^{-2} (light blue). The CTRs are offset by three units for clarity. The grey areas indicate the position of the beam stops used to protect the detectors from the high-intensity Bragg reflections of the TiO_2(110) substrate. The dashed and dotted lines around the (200) reflection indicate the positions of the minima and maxima of the Laue oscillations, respectively. Negative *l* values denote the diffraction signals which have been recorded after transmission through the TiO_2(110) substrate.

The oscillation period in the Laue fringes is inversely proportional to the thickness of the IrO_2(110) film, which can be determined to be 49.8 ± 1.6 Å both at OCP and after ≈26 h of oxygen evolution at 50 mA·cm^{-2}. Since the Laue oscillations arise due to a crystalline finite stack of coherently diffracting unit cells, we conclude that the crystallinity and also the degree of roughness of the IrO_2(110) film has virtually not changed upon the galvanostatic hold.
Before and after the operando synchrotron-based studies the IrO_2(110)-TiO_2(110) model electrode was characterized by STM and XPS. After the operando studies the characterization was conducted twice: directly after introducing the model electrode into the UHV system (cf. **Figure 5d-f**) and after a flash to 670 K in an oxygen atmosphere of 10^{-4} mbar (cf. **Figure 5g-i**). The latter was conducted in order to remove carbon and water contaminations from the surface (clusters visible in **Figure 5f**; also see the XP spectra shown in **Figure S7**). The fitting parameters of the XP spectra are compiled in **Table S3**.

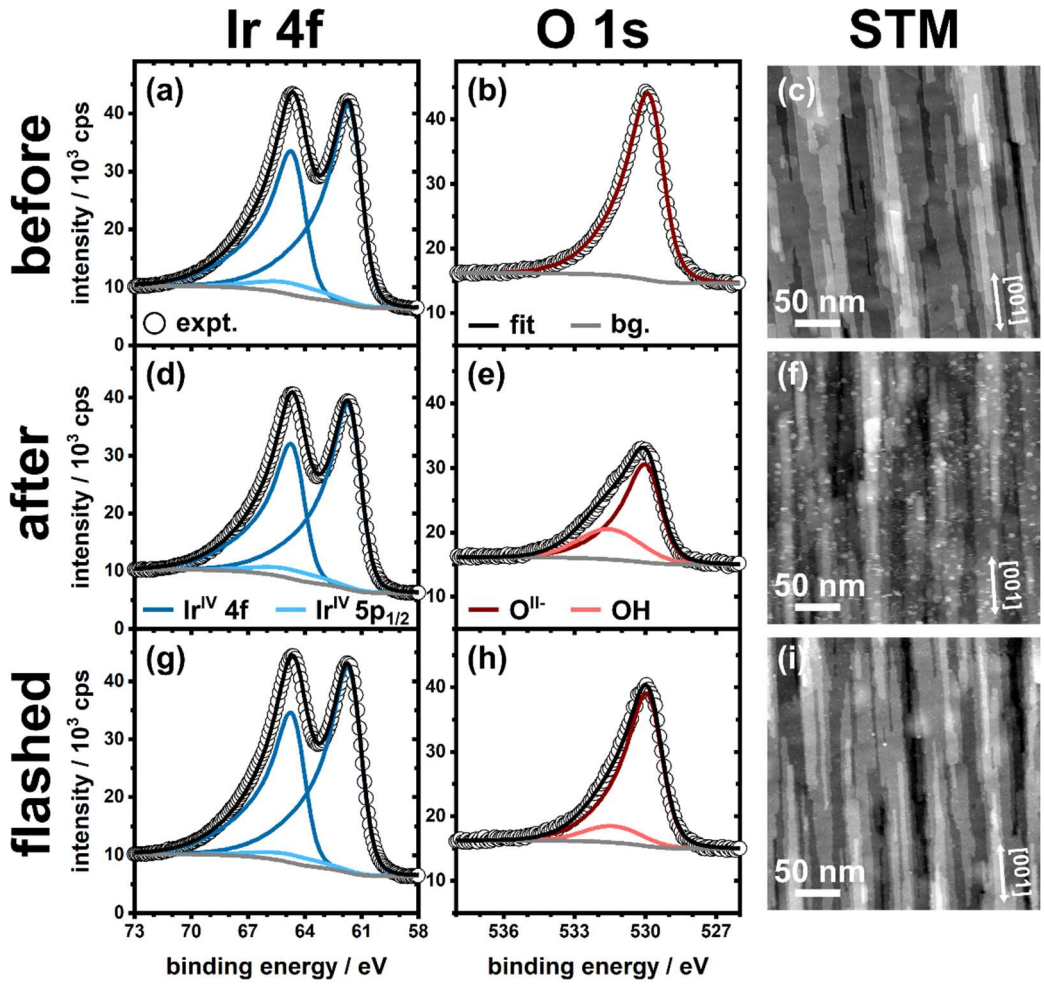

Figure 5: XP spectra and STM images of the IrO_2(110)-TiO_2(110) model electrode (a)-(c) before and (d)-(i) after the synchrotron-based operando studies. XP spectra and STM images after the beamtime were obtained (d)-(f) directly after transfer to the UHV system and (g)-(i) after flashing the model electrode to 670 K in an oxygen atmosphere of 10^{-4} mbar. The legend gives the components included into the fits of the XPS data. Since there is only one component present in the O 1s spectrum before the beamtime (b) a sum spectrum is not shown here. The white double arrows in (c), (f), and (i) indicate the [001] direction.

The Ir 4f spectrum recorded before the operando studies reveals a doublet at binding energies of 61.7 eV and 64.7 eV (cf. **Figure 5a**) which correspond to the Ir $4f_{7/2}$ and Ir $4f_{5/2}$ signals of Ir^{IV} in IrO_2, respectively.[30,31,33,34] In the O 1s spectrum one component is visible at 530.0 eV (cf. **Figure 5b**) which is assigned to bulk oxide O^{II-} of IrO_2.[30,31,34] The STM image (cf. **Figure 5c**) reveals a flat and smooth IrO_2(110) surface with its typical elongated terraces along the [001] direction. Directly after the operando study (≈26 h at 50 mA·cm^{-2}) the intensities of the XP spectra recorded (cf. Figure **5d,e**) are damped compared to the ones recorded before the operando studies. However, the Ir 4f spectrum indicates that only Ir^{IV} of IrO_2 is present (cf. **Figure 5d**) while in the O 1s spectrum in addition to O^{II-} at 530.0 eV a component at a binding energy of 531.5 eV is visible (cf. **Figure 5e**), which is assigned to OH.[31] In the STM image (cf. **Figure 5f**) the elongated terraces are still clearly visible, although the model electrode surface is covered by small clusters due most likely to contamination of the surface with carbon and water (cf. **Figure S7**, middle). To remove these contaminations and improve the resolution of the IrO_2(110) terraces the model electrode was flashed to 670 K in an oxygen atmosphere of 10^{-4} mbar. As a result, the carbon peak in the XP spectrum has vanished (cf. **Figure S7**,

bottom) and the XP spectra gained significantly in intensity (cf. **Figure 5g,h**). In the STM image the clusters disappeared (cf. **Figure 5i**), and the IrO_2(110) surface now looks virtually identical to that taken before the operando studies after preparation (cf. **Figure 5c**). Again, in the Ir 4f spectrum the only species present is Ir^{IV} of IrO_2 (cf. **Figure 5g**) while the O 1s spectrum indicates still low concentration of OH (cf. **Figure 5h**).

4. Discussion

The IrO_2(110)-TiO_2(110)[23] model electrode system enables corrosion studies in the OER potential region without facing potential-induced pitting corrosion[21,22] which was recently found to be the major degradation process in case of the IrO_2(110)-RuO_2(110)/Ru(0001) model electrode system. The IrO_2(110)-TiO_2(110) model system is close to practical coatings of nanostructured thin films used in PEM electrolyzer technology[9] as TiO_2-supported IrO_2 coatings are typically employed (e. g. Elyst Ir75 0480, Umicore, Germany) and the (110) orientation is assumed to be the prevailing orientation.[35] Therefore, any conclusions arising from the study here may be adapted to improve TiO_2-supported OER catalysts. The stability of the IrO_2(110)-TiO_2(110) model electrode was investigated by employing two complementary kinds of operando techniques, thus providing a full picture of the corrosion process. On the one hand, a highly-sensitive SFC-ICP-MS technique is used to quantify Ir dissolution, and therefore provides insights on the anodic corrosion process from the product side. On the other hand, operando synchrotron-based high-energy x-ray scattering techniques (HESXRD, XRR) were employed to follow structural and morphological changes at the atomic scale during anodic polarization. Since the IrO_2(110) film is only 50 Å thick, even subtle structural variations in the film will significantly affect x-ray diffraction and reflectivity, thus making these techniques remarkably sensitive. In addition, techniques such as ex situ STM enabled us to study corrosion-induced morphological changes to the IrO_2(110) film. We should note that the SFC-ICP-MS experiments run at a much lower current density (5 $mA \cdot cm^{-2}$) than the operando x-ray scattering studies (50 $mA \cdot cm^{-2}$), hence direct comparison of SFC-ICP-MS and x-ray scattering results may not be straightforward.

In SFC-ICP-MS we observe a transient behavior of the corrosion process of IrO_2(110), in that the corrosion rate declines with the number of galvanostatic holds (5 $mA \cdot cm^{-2}$) and reaches steady state after the sixth OER pulse (**Figure 1b,c**). It is noteworthy to remember that the corrosion experiments are performed in a dynamic way, in that the galvanostatic hold of 30 s are separated by 4 min each at OCP. This dynamic operation mode is required to avoid clogging of the V-shaped channel of the SFC by bubble formation during the OER. A direct comparison of SCF-ICP-MS experiments for the IrO_2(110)-TiO_2(110) model electrode with measurement of a polycrystalline sputtered IrO_2 films reveals that Ir corrosion during the 30 s OER pulse of single-crystalline IrO_2(110) (0.06 ± 0.01 $ng \cdot cm^{-2}$) is significantly lower than that of the polycrystalline IrO_2 film (0.14 ± 0.01 $ng \cdot cm^{-2}$). This is not surprising and emphasizes that defects in the polycrystalline IrO_2 film, such as grain boundaries, are locations where enhanced corrosion occurs. The importance of crystallinity for the corrosion process was recognized and discussed previously.[36,37]

Using the operando synchrotron-based techniques (HESXRD and XRR) the structural and morphological stability of a single-crystalline IrO_2(110)-TiO_2(110) model electrode was studied during anodic polarization at 50 $mA \cdot cm^{-2}$ for ≈26 h (cf. **Figure 2**). These experiments, in contrast to SFC-ICP-MS, represent a steady state OER operation. Operando XRR indicates the thickness of the IrO_2(110) ultrathin film to be preserved to 49.6 ± 0.1 Å. Therefore, we can

exclude significant uniform thinning of the supported IrO_2(110) film to occur during the corrosion experiment. In HESXRD the integrated intensities of the reflections scatter by less than 2% (with no systematic trend to lower intensity) during the galvanostatic hold (cf. **Figure 3a-c**), so that the IrO_2(110) crystallinity is shown to be preserved. This means in particular that the thickness of the single-crystalline IrO_2(110) film varies by less than 1 Å, consistent with the Laue oscillations on the (2,0) CTR (cf. **Figure 4**) that are also preserved. Based on these findings, we can exclude a considerable disordering of the crystalline structure along the entire film thickness ([110] direction) as well as local dissolution of the single-crystalline IrO_2(110) film. This conclusion is corroborated by ex situ STM experiments before and after the operando studies (cf. **Figure 5**). The STM image recorded after a short flash to 670 K reveals the IrO_2(110) surface to still be uniformly flat and smooth on the atomic scale, and to be practically identical to that of the as-prepared sample (compare **Figure 5c,i**). Neither have the terraces' lateral dimensions changed nor are their plane areas attacked by "pitting corrosion" or localized corrosion. Altogether, these steady state experiments provide clear evidence that significant corrosion has not occurred during ≈26 h of galvanostatic hold at 50 $mA \cdot cm^{-2}$. From the evaluation of the XRR and the Laue oscillation data and the Ir 4f XP spectra we infer an upper limit for the corrosion of 0.10 monolayers (ML) of IrO_2(110) that corresponds to 37 $ng \cdot cm^{-2}$ of Ir. How does this estimate compare with dissolution rate determined by SFC-ICP-MS?

It has previously been recognized that there is a linear correlation between current density and dissolution rate of IrO_2, i.e., the higher the current density during a galvanostatic hold the higher is the amount of IrO_2 dissolved.[20] By the seventh galvanostatic hold (30 s) at 5 $mA \cdot cm^{-2}$ about 0.06 $ng \cdot cm^{-2}$ of IrO_2(110) is dissolved. Assuming a linear correlation of dissolution with current density and time,[20] one could have expected dissolution of 1800 $ng \cdot cm^{-2}$ that corresponds to about 5 monolayer equivalents of IrO_2(110) during ≈26 h at a current density of 50 $mA \cdot cm^{-2}$. However, this value conflicts with the x-ray scattering data which places an upper limit of 0.10 ML equivalent corrosion of IrO_2(110). In the most conservative extrapolation scheme, we assume that dissolution is independent of the current density and depends only on the polarization time. Then extrapolation of the corrosion rate of SFC ICP-MS at 5 $mA \cdot cm^{-2}$ (cf. **Figure 1c**: 60 $pg \cdot cm^{-2}$ in 30 s) to 26 h results in a total corrosion of 187 $ng \cdot cm^2$, that corresponds to 0.50 ML equivalent of IrO_2. This value is still five times higher than the upper limit of 0.10 ML as determined by XRR and HESXRD experiments. Therefore, we favor an alternative interpretation, namely that corrosion depends critically on the operation conditions, meaning that under dynamic operation (as encountered with SFC-ICP-MS) the corrosion rate is significantly higher than under steady state conditions (as encountered in the XRR, HESXRD experiments). Here further operando XRR and SXRD experiments are required, where steady state and dynamic operation are directly compared.

Binninger et al.[38] proposed from basic thermodynamic considerations that "any metal oxide must become unstable under oxygen evolution conditions irrespective of the pH value" due to the lattice oxygen evolution reaction (LOER) $2O^{2-} \rightarrow O_2 + 4e^-$. Since virtually no corrosion is observed in the long-term operando synchrotron-based experiments, the proposed LOER over IrO_2(110) is likely to be suppressed for kinetics reasons, consistent with oxygen isotope labeling experiments[39,40] where only surface oxygen of IrO_2 has shown to participate in the OER reaction. A recent ab initio thermodynamics and kinetics study has shown that the lattice oxygen mechanism can outperform the conventional mechanism when many Ir vacancies are present on the IrO_2(110) surface.[41]

IrO_2(110) films supported on TiO_2(110) have shown extraordinary stability under strong cathodic conditions as well.[31] It was shown that at cathodic potentials as low as −1.2 V vs. RHE the IrO_2(110) layer does neither lose crystallinity nor does the layer swell due to proton incorporation.[31] After cathodic polarization down to −1.2 V vs. RHE, ex situ XPS indicated that Ir remains exclusively in the +IV oxidation state. Therefore, the extraordinary cathodic stability of ultrathin IrO_2(110) film needs to be traced to kinetic reasons that are not controllable by the electrode potential. One could anticipate that anodic and cathodic stability might share a common reason such as purely chemically steps that are rate-determining in the reaction mechanisms. This hypothesis deserves further attention in particular from the theoretical side and could perhaps provide key to understanding the extraordinary stability of IrO_2(110) films under harsh electrochemical reaction conditions. A recent first principles study[19] predicted that a surface-bound IrO_2OH species is an important reaction intermediate in the corrosion process of IrO_2(110). Actually, the first step to produce this intermediate is a pure chemical step which is characterized by a high activation barrier of 1.7 eV. This could be the rate-determining chemical step mentioned above. The high barrier of 1.7 eV is also in agreement with the extraordinarily low corrosion rate of single-crystalline IrO_2(110) film observed in the present experiments. In the same theory study some rationale for the accelerated dissolution under dynamic operation conditions can be found. While for high electrode potentials IrO_2OH turns out to be the most important reaction intermediate in the dissolution process, at lower electrode potential the $Ir(OH)_3$ intermediate is dominating the corrosion process. This switch in prevailing reaction intermediate may explain the observed higher dissolution rate under dynamic reaction conditions, although further theoretical calculations are required.

The operando synchrotron-based x-ray scattering techniques are surprisingly sensitive to Ir corrosion of about 0.10 ML IrO_2(110) in ≈26 h, i.e. 0.4 $pg \cdot cm^{-2} \cdot s^{-1}$. This high sensitivity is accomplished by the long polarization time period of ≈26 h, at the expense of a lower time resolution where kinetic information can hardly be derived. However, these operando synchrotron-based x-ray scattering techniques allow the identification of structural and morphological changes upon anodic polarization with a resolution of 0.10 ML of IrO_2(110). Quite in contrast, SFC-ICP-MS is very sensitive, with a time resolution on the second scale. With this unique technique, the corrosion rate can be followed as function of time, providing kinetic data that can be modeled by microkinetics, if the reaction mechanism is known. Here, the results from synchrotron-based operando x-ray scattering techniques might provide a promising starting point towards a mechanistic understanding of anodic corrosion.

5. Conclusions

We introduced a powerful and unique combination of operando techniques, namely SCF-ICP-MS and synchrotron-based high-energy x-ray scattering techniques, to follow both the corrosion rate and structural changes occurring during the anodic corrosion of model electrodes: a 50 Å thick single-crystalline IrO_2(110) films supported on slightly bulk-reduced TiO_2(110) single crystal. Both methods are very sensitive to anodic corrosion: while by SFC-ICP-MS the corrosion rate can be determined with a time resolution on the second scale, thus providing high quality kinetic data, with high-energy XRR and SXRD the structural changes can be followed with a spatial resolution on the atomic scale. This combination of techniques together with dedicated single-crystalline model electrodes is capable of pushing our atomistic understanding of anodic corrosion. We have shown that the IrO_2(110) film supported on TiO_2(110) single crystal remains practically intact on the atomic scale upon a galvanostatic

hold (50 $mA \cdot cm^{-2}$) for ≈ 26 h. Together with the extraordinary stability of the $IrO_2(110)$-$TiO_2(110)$ model electrode under strongly reducing cathodic potentials of −1.2 V vs. RHE, we conclude that the Ir-O bonds can hardly be attacked by protons cathodically nor by water anodically. The anodic dissolution rate (although very small) seems to depend on the operation conditions: under dynamic conditions, as encountered in the SFC-ICP-MS experiments, the corrosion rate is significantly higher than under steady state conditions as encountered in XRR and SXRD experiments. This finding should be considered for future design of IrO_2-based electrocatalysts, when employed for the production of green hydrogen from intermittent renewable sources such as solar and wind. We expect studies of single-crystalline model electrodes employing operando high energy x-ray scattering and diffraction techniques together with operando ICP-MS to hold promise for pushing our microscopic understanding of anodic corrosion processes.

Author Information

Notes

The authors declare no competing financial interest.

Associated Content

Supporting Information

The Supporting Information is available free of charge…:

- SE micrographs and XPS data of the $IrO_2(110)$-$TiO_2(110)$ model electrode before and after the SFC-ICP-MS experiments
- diffraction pattern and corresponding in-plane diffraction map of the $IrO_2(110)$-$TiO_2(110)$ model electrode; XRR data and obtained fitting parameters for all scans conducted; additional evaluations of the HESXRD data; plots of the (0,2) CTR for different conditions
- XPS data of the $IrO_2(110)$-$TiO_2(110)$ model electrode before and after the synchrotron-based studies

Acknowledgements

We thank financial support by the BMBF (project: 05K2016-HEXCHEM), the Swedish Research Council (2016-05234), and the DFG (SPP2080: Ov21-16). S.C. and D.E.L. thank the DFG for financial support within the grant CH1763/3-1 as part of the Priority Program SPP2080 “Catalysts and reactors under dynamic conditions for energy storage and conversion”. S.C. also thanks the DFG for financial support within the grant CH1763/4-1. We acknowledge DESY (Hamburg, Germany), a member of the Helmholtz Association HGF, for the provision of experimental facilities. Beamtime was allocated for proposal II-20190755 EC.

References

(1) Crabtree, G.W.; Dresselhaus, M.S.; Buchanan, M.V. The Hydrogen Economy. *Phys. Today* **2004**, *57*, 39-44.

(2) Schlögl, R. Put the Sun in the Tank: Future Developments in Sustainable Energy Systems. *Angew. Chem. Int. Ed.* **2019**, *58*, 343-348.

(3) Schalenbach, M.; Tjarks, G.; Carmo, M.; Lueke, W.; Mueller, M.; Stolten, D. Acidic or Alkaline? Towards a New Perspective on the Efficiency of Water Electrolysis. *J. Electrochem. Soc.* **2016**, *163*, F3197-F3208.

(4) Carmo, M.; Fritz, D.L.; Mergel, J.; Stolten, D. A Comprehensive Review on PEM Water Electrolysis. *Int. Hydrog. Energy* **2013**, *38*, 4901-4934.

(5) Katsounaros, I.; Cherevko, S.; Zeradjanin, A.R.; Mayrhofer, K.J.J. Oxygen Electrochemistry as a Cornerstone for Sustainable Energy Conversion. *Angew. Chem. Int. Ed.* **2014**, *53*, 102-121.

(6) Masa, J.; Andronescu, C.; Schuhmann, W. Electrocatalysis as the Nexus for Sustainable Renewable Energy: The Gordian Knot of Activity, Stability, and Selectivity. *Angew. Chem. Int. Ed.* **2020**, *59*, 15298-15312.

(7) Yu, J.; He, Q.; Yang, G.; Zhou, W.; Shao, Z.; Ni, M. Recent Advances and Prospective in Ruthenium-Based Materials for Electrochemical Water Splitting. *ACS Catal.* **2019**, *9*, 9973-10011.

(8) Ayers, K.E.; Renner, J.N.; Danilovic, N.; Wang, J.X.; Zhang, Y.; Maric, R.; Yu, H. Pathways to Ultra-Low Platinum Group Metal Catalyst Loading in Proton Exchange Membrane Electrolyzers. *Catal. Today* **2016**, *262*, 121-132.

(9) Bernt, M.; Hartig-Weiß, A.; Tovini, M.F.; El-Sayed, H.A.; Schramm, C.; Schröter, J.; Gebauer, C.; Gasteiger, H.A. Current Challenges in Catalyst Development for PEM Water Electrolyzers. *Chem. Ing. Tech.* **2020**, *92*, 31-39.

(10) Norskov, J.K.; Rossmeisl, J.; Logadottir, A.; Lindqvist, L.; Kitchin, J.R.; Bligaard, T.; Jonsson, H. Origin of the Overpotential for Oxygen Reduction at a Fuel-Cell Cathode. *J. Phys. Chem. B* **2004**, *108*, 17886-17892.

(11) Rossmeisl, J.; Qu, Z.-W.; Zhu, H.; Kroes, G.-J.; Norskov, J.K. Electrolysis of Water on Oxide Surfaces. *J. Electroanal. Chem.* **2007**, *607*, 83-89.

(12) Kuo, D.-Y.; Kawasaki, J.K.; Nelson, J.N.; Kloppenburg, J.; Hautier, G.; Shen, K.M.; Schlom, D.G.; Suntivich, J. Influence of Surface Adsorption on the Oxygen Evolution Reaction on IrO_2(110). *J. Am. Chem. Soc.* **2017**, *139*, 3473-3479.

(13) Exner, K.S.; Sohrabnejad-Eskan, I.; Over, H. A Universal Approach to Determine the Free Energy Diagram of an Electrocatalytic Reaction. *ACS Catal.* **2018**, *8*, 1864-1879.

(14) Rao, R.R.; Kolb, M.J.; Giordano, L.; Pedersen, A.F.; Katayama, Y.; Hwang, J.; Mehta, A.; You, H.; Lunger, J.R.; Zhou, H.; Halck, N.B.; Vegge, T.; Chorkendorff, I.; Stephens, I.E.L.; Shao-Horn, Y. Operando Identification of Site-Dependent Water Oxidation Activity on Ruthenium Dioxide Single-Crystal Surfaces. *Nat. Catal.* **2020**, *3*, 516-525.

(15) Man, I.C.; Su, H.-Y.; Calle-Vallejo, F.; Hansen, H.A.; Martinez, J.I.; Inoglu, N.G.; Kitchin, J.; Jaramillo, T.F.; Norskov, J.K.; Rossmeisl, J. Universality in Oxygen Evolution Electrocatalysis on Oxide Surfaces. *ChemCatChem* **2011**, *3*, 1159-1165.

(16) Over, H. Fundamental Studies of Planar Single-Crystalline Oxide Model Electrodes (RuO_2, IrO_2) for Acidic Water Splitting. *ACS Catal.* **2021**, *11*, 8848-8871.

(17) Frydendal, R.; Paoli, E.A.; Knudsen, B.P.; Wickman, B.; Malacrida, P.; Stephens, I.E.L.; Chorkendorff, I. Benchmarking the Stability of Oxygen Evolution Reaction Catalysts: The Importance of Monitoring Mass Losses. *ChemElectroChem* **2014**, *1*, 2075-2081.

(18) Cherevko, S.; Geiger, S.; Kasian, O.; Kulyk, N.; Grote, J.-P.; Savan, A.; Shrestha, B.R.; Merzlikin, S.; Breitbach, B.; Ludwig, A.; Mayrhofer, K.J.J. Oxygen and Hydrogen Evolution Reactions on Ru, RuO_2, Ir, and IrO_2 Thin Film Electrodes in Acidic and Alkaline Electrolytes: A Comparative Study on Activity and Stability. *Catal. Today* **2016**, *262*, 170-180.

(19) Zagalskaya, A.; Alexandrov, V. Mechanistic Study of IrO_2 Dissolution during the Electrocatalytic Oxygen Evolution Reaction. *J. Phys. Chem. Lett.* **2020**, *11*, 2695-2700.

(20) Kasian, O.; Grote, J.-P.; Geiger, S.; Cherevko, S.; Mayrhofer, K.J.J. The Common Intermediates of Oxygen Evolution and Dissolution Reactions during Water Electrolysis on Iridium. *Angew. Chem. Int. Ed.* **2018**, *57*, 2488-2491.

(21) Weber, T.; Pfrommer, J.; Abb, M.J.S.; Herd, B.; Khalid, O.; Rohnke, M.; Lakner, P.H.; Evertsson, J.; Volkov, S.; Bertram, F.; Znaiguia, R.; Carla, F.; Vonk, V.; Lundgren, E.; Stierle, A.; Over, H. Potential-Induced Pitting Corrosion of an IrO_2(110)-RuO_2(110)/Ru(0001) Model Electrode under Oxygen Evolution Reaction Conditions. *ACS Catal.* **2019**, *9*, 6530-6539.

(22) Weber, T.; Ortmann, T.; Escalera-Lopez, D.; Abb, M.J.S.; Mogwitz, B.; Cherevko, S.; Rohnke, M.; Over, H. Visualizing Potential-Induced Pitting Corrosion of Ultrathin Single-Crystalline IrO_2(110) Films on RuO_2(110)/Ru(0001) under Electrochemical Water Splitting Conditions. *ChemCatChem* **2020**, *12*, 855-866.

(23) Abb, M.J.S.; Weber, T.; Glatthaar, L.; Over, H. Growth of Ultrathin Single-Crystalline IrO_2(110) Films on a TiO_2(110) Single Crystal. *Langmuir* **2019**, *35*, 7720-7726.

(24) Klemm, S.O.; Topalov, A.A.; Laska, C.A.; Mayrhofer, K.J.J. Coupling of a High Throughput Microelectrochemical Cell with Online Multielemental Trace Analysis by ICP-MS. *Electrochem. Commun.* **2011**, *13*, 1533-1535.

(25) Gustafson, J.; Shiplin, M.; Zhang, C.; Stierle, A.; Hejral, U.; Ruett, U.; Gutowski, O.; Carlsson, P.-A.; Skoglundh, M.; Lundgren, E. High-Energy Surface X-ray Diffraction for Fast Surface Structure Determination. *Science* **2014**, *343*, 758-761.

(26) Hejral, U.; Müller, P.; Shiplin, M.; Gustafson, J.; Franz, D.; Shayduk, R.; Rütt, U.; Zhang, C.; Merte, L.R.; Lundgren, E.; Vonk, V.; Stierle, A. High-Energy X-Ray Diffraction from Surfaces and Nanoparticles. *Phys. Rev. B* **2017**, *96*, 195433.

(27) Foresti, M.L.; Pozzi, A.; Innocenti, M.; Pezzatini, G.; Loglio, F.; Salvietti, E.; Giusti, A.; D'Anca, F.; Felici, R.; Borgatti, F. In situ X-Ray Analysis under Controlled Potential Conditions: An Innovative Setup and Its Application to the Investigation of Ultrathin Films Electrodeposited on Ag(111). *Electrochim. Acta* **2006**, *51*, 5532-5539.

(28) Zhang, F.; Evertsson, J.; Bertram, F.; Rullik, L.; Carla, F.; Langberg, M.; Lundgren, E.; Pan, J. Integration of Electrochemical and Synchrotron-Based X-Ray Techniques for In-Situ Investigation of Aluminum Anodization. *Electrochim. Acta* **2017**, *241*, 299-308.

(29) Cherevko, S. Electrochemical Dissolution of Noble Metals Native Oxides. *J. Electroanal. Chem.* **2017**, *787*, 11-13.

(30) Abb, M.J.S.; Weber, T.; Langsdorf, D.; Koller, V.; Gericke, S.M.; Pfaff, S.; Busch, M.; Zetterberg, J.; Preobrajenski, A.; Grönbeck, H.; Lundgren, E.; Over, H. Thermal Stability of Single-Crystalline IrO_2(110) Layers: Spectroscopic and Adsorption Studies. *J. Phys. Chem. C* **2020**, *124*, 15324-15336.

(31) Weber, T.; Vonk, V.; Abb, M.J.S.; Evertsson, J.; Sandroni, M.; Drnec, J.; Stierle, A.; Lundgren, E.; Over, H. Extraordinary Stability of IrO_2(110) Ultrathin Films Supported on TiO_2(110) under Cathodic Polarization. *J. Phys. Chem. Lett.* **2020**, *11*, 9057-9062.

(32) Björck, M.; Andersson, G. *GenX*: An Extensible X-Ray Reflectivity Refinement Program Utilizing Differential Evolution. *J. Appl. Crystallogr.* **2007**, *40*, 1174-1178.

(33) Pfeifer. V.; Jones, T.E.; Velasco-Velez, J.J.; Massue, C.; Arrigo, R.; Teschner, D.; Girgsdies, F.; Scherzer, M.; Greiner, M.T.; Allan, J.; Hashagen, M.; Weinberg, G.; Piccinin, S.; Hävecker, M.; Knop-Gericke, A.; Schlögl, R. The Electronic Structure of Iridium and Its Oxides. *Surf. Interface Anal.* **2016**, *48*, 261-273.

(34) Freakley, S.J.; Ruiz-Esquius, J.; Morgan, D.J. The X-Ray Photoelectron Spectra of Ir, IrO_2 and $IrCl_3$ Revisited. *Surf. Interface Anal.* **2017**, *49*, 794-799.

(35) Novell-Leruth, G.; Carchini, G.; Lopez, N. On the Properties of Binary Rutile MO_2 compounds, M= Ir, Ru, Sn, and Ti: A DFT Study. *J. Chem. Phys.* **2013**, *138*, 1947706.

(36) Danilovic, N.; Subbaraman, R.; Chang, K.-C.; Chang, S. H.; Kang, Y. J.; Snyder, J.; Paulikas, A. P.; Strmcnik, D.; Kim, Y.-T.; Myers, D.; Stamenkovic, V. R.; Markovic, N. M. Activity-Stability Trends for the Oxygen Evolution Reaction on Monometallic Oxides in Acidic Environments. *J. Phys. Chem. Lett.* **2014**, *5*, 2474-2478.

(37) Geiger,S.; Kasian, O.; Ledendecker, M.; Pizzutilo, E.; Mingers, A. M.; Fu, W. T.; Diaz-Morales, O.; Li, Z.; Oellers, T.; Fruchter, L.; Ludwig, A.; Mayrhofer, K. J. J.; Koper, M. T. M.; Cherevko, S. The Stability Number as a Metric for Electrocatalyst Stability Benchmarking. *Nat. Catal.* **2018**, *1*, 508-515.

(38) Binninger, T.; Mohamed, R.; Waltar, K.; Fabbri, E.; Levecque, P.; Kötz, R.; Schmidt, T.J. Thermodynamic Explanation of the Universal Correlation between Oxygen Evolution Activity and Corrosion of Oxide Catalysts. *Sci. Rep.* **2015**, *5*, 12167.

(39) Fierro, S.; Nagel, T.; Baltruschat, H.; Comninellis, C. Investigation of the Oxygen Evolution Reaction on Ti/IrO_2 Electrodes Using Isotope Labelling and On-Line Mass Spectrometry. *Electrochem. Commun.* **2007**, *9*, 1969-1974.

(40) Schweinar, K.; Gault, B.; Mouton, I.; Kasian, O. Lattice Oxygen Exchange in Rutile IrO_2 during the Oxygen Evolution Reaction. *J. Phys. Chem. Lett.* **2020**, *11*, 5008-5014.

(41) Zagalskaya, A.; Evazzade, I.; Alexandrov, V. Ab Initio Thermodynamics and Kinetics of the Lattice Oxygen Evolution Reaction in Iridium Oxides. *ACS Energy Lett.* **2021**, *6*, 1124-1133.

Graphical Abstract: